

# The effects of thermal stress and fluid pressure on induced seismicity during stimulation to production within fractured reservoirs

Ghazal Izadi and Derek Elsworth

Department of Energy and Mineral Engineering, EMS Energy Institute and G3 Center, Pennsylvania State University, University Park Pennsylvania, 16802, USA

## ABSTRACT

We use a continuum model of reservoir evolution to explore the interaction of coupled thermal, hydraulic and chemical processes that influence the evolution of seismicity within a fractured reservoir from stimulation to production. Events occur from energy release on seeded fractures enabling moment magnitude, frequency and spatial distribution to be determined with time. Event magnitudes vary in the range  $-2$  to  $+2$  with the largest event size ( $\sim 2$ ) corresponding to the largest fracture size ( $\sim 500$  m) and a prescribed stress drop of 9 MPa. Modelled  $b$ -values ( $\sim 0.6$ – $0.7$ ) also correspond to observations ( $\sim 0.7$ – $0.8$ ) for response in the Cooper Basin

(Australia). We track the hydrodynamic and thermal fronts to define causality in the triggering of seismicity. The hydrodynamic front moves twice as fast as the thermal front and envelops the triggered seismicity at early time (days to month) – with higher flow rates correlating with larger magnitude events. For later time (month to years), thermal drawdown and potentially chemical influences principally trigger the seismicity, but result in a reduction in both the number of events and their magnitudes.

Terra Nova, 25, 374–380, 2013

## Introduction

Fluid injection at pressures intermediate between the minimum principal stress and the Coulomb stress will induce shear failure within enhanced geothermal reservoirs (EGS) (Hubbert and Rubey, 1959; Segall, 1989; Majer and Peterson, 2007; Majer *et al.*, 2007) and may trigger seismicity (Yerkes and Castle, 1976; Grasso and Wittlinger, 1990). Influence of fluid pressures on failure is exacerbated by the significant changes in total stress that may result from thermal drawdown and potentially from chemical effects within the reservoir. Shear failure may occur aseismically, but is also manifest as microseismic activity in many cases.

In these cases, the induced seismicity results from fluid injection and is expected to migrate within the reservoir with time as driven by the various interactions of thermal, hydraulic, mechanical and chemical (THMC) processes, which also migrate through the reservoir on dif-

ferent length-scales and time-scales (Walsh, 1965; Goodman, 1976; Barton *et al.*, 1985; Taron and Elsworth, 2009; Elsworth and Yasuhara, 2010). Defining the potential causes of induced seismic activity due to production from engineered geothermal systems is a significant concern – both to understand mechanisms and to mitigate damaging consequences. The size of the resulting seismic event is defined by the total energy release that in turn relates to the stress drop and how fast it fails (Brune and Thatcher, 2002).

In the following, we use a continuum model of reservoir evolution subject to coupled THMC processes (Taron and Elsworth, 2009) to explore the evolution of production-induced seismicity in a prototypical EGS reservoir. In this study, we define the relationship between the magnitudes of induced seismic events and the applied fluid injection rates as well as the evolution of thermal stress. Our focus is to determine dominant behaviours controlling the triggering of induced seismicity that is unique in comparison with previous studies. We show that induced seismicity is modulated by hydraulic, thermal and chemical processes, which also migrate through the reservoir (Taron and Elsworth, 2009; Elsworth and Yasuhara, 2010). We

then explore how pore pressure and thermal stress can be linked to the seismic frequency–magnitude distribution, which is described by its slope, the  $b$ -value.

## Model dimension and description

### Reservoir and fracture network characterization

We assume a doublet geometry (500 m spacing) and the dimension of the reservoir volume in the model is  $2000 \times 1000 \times 100$  m<sup>3</sup> for the half-symmetry. Fig. 1 is the representative of the Cooper Basin geothermal field. The THMC model evaluates the evolution of flow rate, pressure and temperature distribution during stimulation. The applied injection pressure and temperature are assumed to be equal to 39.8 MPa and 70 °C. Reservoir pressure and temperature are assumed to be 29.8 MPa and 250 °C respectively. Boundary stresses and the values of the solid medium properties utilized in the simulation for this case are defined in Table 1. Reactive composition of the host reservoir rock is presented in Table 2.

Calcite and amorphous silica are expected to be the minerals primarily responsible for permeability change due to precipitation and dissolution.

Correspondence: Ghazal Izadi, Department of Energy and Mineral Engineering, EMS Energy Institute and G3 Center, Pennsylvania State University, University Park, PA 16802, USA. Tel.: 001 814 777 4099; e-mail: ghazal.izadi@gmail.com and gui2@psu.edu

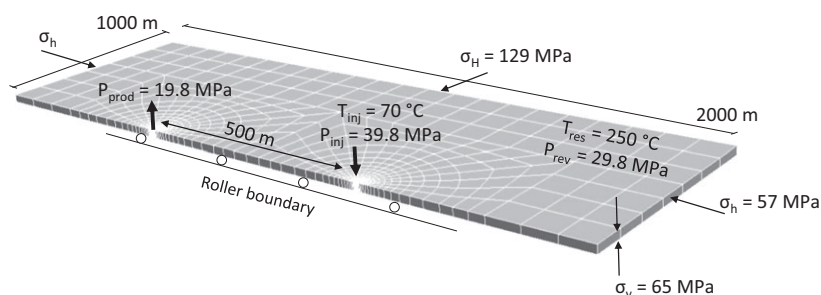


**Fig. 1** Geometric layout and boundary conditions of enhanced geothermal reservoirs as used in the simulation.

**Table 1** Parameters utilized in the simulation.

Parameter	Unit	Cooper Basin
$S_{zz}$	MPa	65
$S_{yy}$	MPa	57
$S_{xx}$	MPa	129
Fluid pressure ( $P_{inj}$ )	MPa	39.8
Injection temperature	°C	70
Reservoir temperature	°C	250
Bulk modulus of intact rock ( $K_m$ )	GPa	17
Cohesion	MPa	10
Poisson's ratio ( $\nu$ )	–	0.27
Bulk modulus of fluid ( $k_f$ )	GPa	8
Bulk modulus of solid grain ( $K_s$ )	GPa	54.5
Internal friction angle ( $\phi$ )	–	35
Residual friction angle ( $\beta$ )	–	11
Coefficient of thermal expansion ( $\alpha_T$ )	1/°C	$1.2 \times 10^{-5}$
Thermal conductivity ( $\lambda$ )	W/mK	2.9
Heat capacity ( $c_p$ )	J/kgK	918
Porosity within fractures ( $\phi$ )	–	0.3

**Table 2** Initial volume fraction of reactive minerals in host reservoir.

Mineral	Volume fraction of solid rock	
	Granodiorite	Fractured vein
Anorthite	0.33	–
Calcite	0.02	0.31
Chlorite	–	0.23
K-Feldspar	0.17	–
Quartz	0.34	0.17
Amorphous Silica	–	–

Other likely minerals are also followed, as listed in Table 2. Rate constants for precipitation/dissolution and mineral reactive surface areas of these common minerals are available in the literature (Kovac *et al.*, 2006; Xu and Pruess, 2001), and were utilized as in Xu and Pruess (2004).

The present model uses the vertical stress and two horizontal principal stresses, which are designated as the

maximum and minimum principal stresses. In the process of stimulation, fluid pressure is increased within the near-wellbore rock volume with low permeability, causing hydro-shear displacement on some of the pre-existing fractures (fracture propagation is not considered). Discrete penny-shaped fractures are seeded within the reservoir volume and fractures are distributed within the volume with multiple orientations and a Gaussian distribution of lengths (1–500 m). As the large fractures (200–500 m), which represent the weaker planes in the system, are limited (large spacing) and have the largest probability to generate the seismic events during change of pore pressure as well as temperature along these planes, we can say that the greatest impacts are caused only by large fractures and large fractures/faults capable of generating the larger magnitude events. Thus, the

Gaussian distribution is used for the small infill fractures, which when added to the large fractures give an extended tail representing a log-normal-like distribution. Then, we can describe the combinations of distributions for these variables using the mathematical probability function, as we have different independent variables. The maximum length fractures will transit multiple blocks and the smallest fractures will be contained within a single finite difference block. An average fracture density of  $\sim 0.1 \text{ m}^{-1}$  is applied to the reservoir and fracture spacing is defined based on fracture size (10–500 m), so that larger fractures are more widely spaced – to recover the prescribed fracture density (Fig. 2).

### THMC model

Here, we focus on the complex interaction of coupled THMC processes that influence the evolution of EGS reservoirs and describe the dominant behaviours that progress with the evolution of the reservoir. We apply a coupled THMC model (Taron *et al.*, 2009) with static–dynamic frictional strength-drop to determine energy release for fractures of different size embedded within an elastic medium.

Change of stress state is calculated from the pore pressures, thermal drawdown and chemical effects within FLAC<sup>3D</sup>-TOUGHREACT (Taron and Elsworth, 2009). Shear failure calculations are handled with FLAC<sup>3D</sup> utilizing a Mohr–Coulomb failure criterion (fracture propagation is not considered). The friction angle on fractures is assumed to be constant (35°) and during failure, the maximum shear stress drop ( $\sim 9.0 \text{ MPa}$ ) is prescribed to represent the residual strength. This model calculates the flow rate, pressure and temperature distribution during stimulation. The changes in pressure and temperature induce displacements that consequently lead to a new change in pressure distribution.

These include short-term response where effective stresses and thermal quenching are expected to dominate the behaviour of the reservoir and are influenced by the local structure in the rock and orientation of pre-existing fractures. Typical behaviours

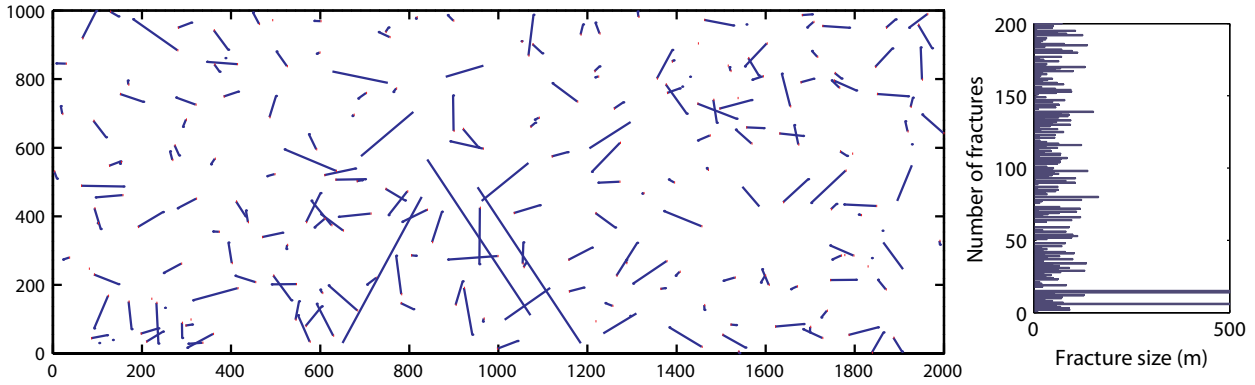


Fig. 2 Fracture data utilized in the simulation. Fracture density of  $0.1 \text{ m}^{-1}$  and these vary in length from 1 to 500 m. Fracture distribution by location (left) and fracture distribution by size (right).

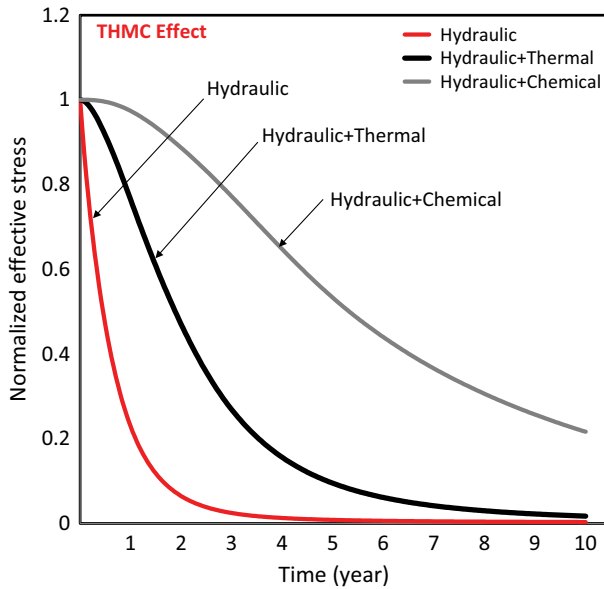


Fig. 3 Normalized effective stress vs. time at 50 m from injection point. Hydraulic, thermal and chemical effects are separately illustrated during 10 years production and their influence on triggering seismicity. Red solid line, injection pressure assumed 39.8 MPa and reservoir pressure is 29.8 MPa and temperature of injection is assumed the same as rock temperature (250 °C) and no chemical reaction occurs. Black dashed line, both pressure and temperature changed; injection pressure is 39.8 MPa and reservoir pressure is 29.8 MPa, injection temperature is 70 °C and reservoir temperature is 250 °C, again no chemical reaction. Grey dashed line, injection pressure is 39.8 MPa and reservoir pressure is 29.8 MPa, injection temperature is the same as reservoir temperature (250 °C), chemical reaction is considered (injection fluid component illustrated in Table 2).

include the reduction in local mean stresses and the development of shear fracturing principally on pre-existing fractures. The very short-term response (days to months) (Fig. 3) is controlled by fluid pressure and effective stress effects (HM).

Throughout the evolution of the reservoir, these coupled effects con-

trol the development of permeability, of heat-transfer area, and thereby thermal output of the reservoir, together with the evolution of induced seismicity. We applied different models to illustrate the timing of THMC effects separately (Fig. 3). Thus, we note the sequencing of fluid pressure effects as fastest-acting fol-

lowed by thermal stresses, then chemical effects influence the timing and migration of changes in effective stress within reservoirs as illustrated in Fig. 3. As seismicity is indexed to changes in effective stresses, these rates of change will influence triggering within the reservoir.

**Observation and calibration**

We examine the performance of our models against the observed response of the Cooper Basin geothermal field (Australia) and specifically the progress of seismicity as the reservoir is developed in terms of rates, magnitudes and locations (Baisch *et al.*, 2006).

**Evolution of moment magnitude**

The potential energy released within reservoirs for different fracture spacing is defined based on the evaluation of the elastic energy released from the failure of large penny-shaped fractures. Shear stress drop is calculated in FLAC<sup>3D</sup> as a function of normal stress and pore pressure for a variety of uniform fracture spacings at different locations within the reservoir.

Shear stress builds in the early time (<1 month) and reaches a maximum magnitudes in the range ~28 MPa as defined by prescribed peak strengths. This peak strength is defined by a cohesion of 10 MPa, peak friction angle of 35 and during failure, the maximum shear stress drop (~9.0 MPa) is prescribed to represent the residual strength. Then, we

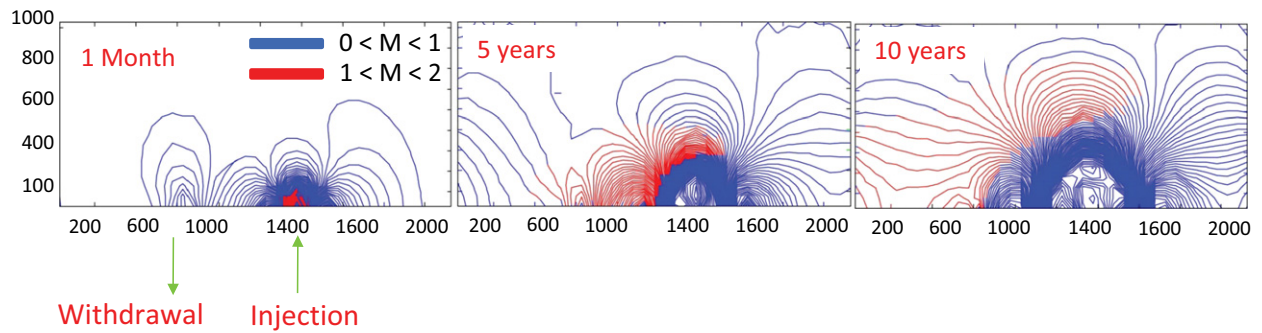


**Fig. 4** The evolution of moment magnitude in the Cooper Basin enhanced geothermal reservoir over 10 years of simulation. Solid lines illustrate the failure in each location of the reservoir. Blue region illustrates smallest event magnitude and red region illustrates the largest potential energy that is released in different locations due to combined thermal, mechanical and chemical effects.

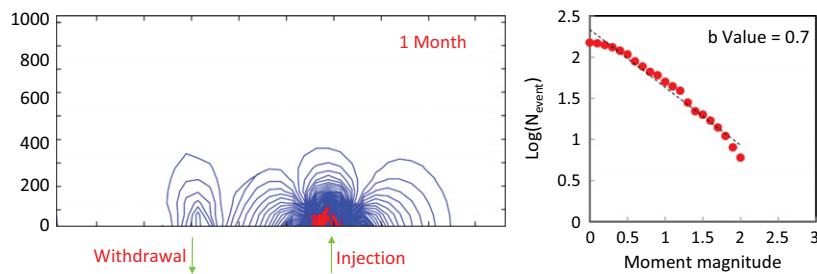


**Fig. 5** Evolution of moment magnitude in the Cooper Basin enhanced geothermal reservoir after 1 month stimulation (left). Number of events as a function of magnitude indicating  $b$ -value of 0.7 and moment magnitude range 0–2 (right).

calculate the potential energy release,  $E_p$ , from failure of penny-shaped fractures due to a stress drop  $\Delta\tau$  at different locations within the reservoir. This relation is defined as  $E_p = 2\Delta\tau^2 a^3 / 3G$ , where  $a$  is the radius of the fracture in the plane and  $G$  is shear modulus.

Energy release from fractures is most conveniently represented as a moment magnitude (Keylis-Borok, 1959; Aki, 1967; Kanamori, 1977). The moment magnitude relation is defined as (Purcaru and Berckemer, 1978):  $\log M_0 = 1.5M_s + 9.1$ , where  $M_0$  is seismic moment and  $M_s$  is moment magnitude. In this model,  $M_0$  is seismic energy, which is derived from the elastic energy released by shear on pre-existing fractures. This relation allows us to determine both the spatial and temporal evolution of moment magnitude in EGS reservoirs and such moment magnitude ( $M_s$ ) varies from  $-2$  to  $+2$  for the largest fracture size ( $\sim 500$  m).

We then use a stress–strain fracture criterion to determine the total strain energy available for release –

this energy is assumed to be shed seismically. During the rupture process, the shear stress drops an amount  $\Delta\tau$  from an initial value of  $\tau_i$  to final value  $\tau_f$ , then we can define an expression for total energy  $E_T = \int \Delta\tau^T \Delta\epsilon dV$ , where strain changes from an initial value of  $\epsilon_i$  to a final value  $\epsilon_f$  where  $V$  is volume of the matrix. Here, we introduce a relation to determine the number of events, which occur during the failure process based on potential and total energy as  $N_{\text{event}} = E_T / E_p$ , where  $N_{\text{event}}$  is the number of seismic events,  $E_T$  is the total energy of the matrix block and  $E_p$  is the potential energy released from the fractures.

Here, the energy release of fractures within the reservoir determines the evolution of seismic event magnitude. The release of seismic energy (stress drop = 9 MPa), which is generated in the Cooper Basin EGS reservoir due to thermal, mechanical and chemical effects when seeded with fractures (1–500 m), is illustrated in Fig. 4. This outcome indicates that during stimulation, the

potential energy within the reservoir containing fracture networks is released gradually and extends far from injection. The characteristic event magnitude distribution that occurs has a stress drop of  $\sim 9$  MPa, which implies the occurrence of larger magnitude events ( $\sim 1$ – $2$ ) near injection at early times (days to month) during the stimulation. This process is controlled by the population of fracture sizes and the stress drop.

#### Empirical relation for triggering seismicity

The  $b$ -value recovered from the analysis is used to calibrate the model against field data. The  $b$ -value is an observable parameter from accumulated seismic observations and may be used to calibrate models – as is attempted here. Aki (1981) speculated that the  $b$ -value relates to the fractal geometry of the fault plane assemblage and argued that the  $\log N$ – $M$  relation for earthquakes is equivalent to a fractal distribution.

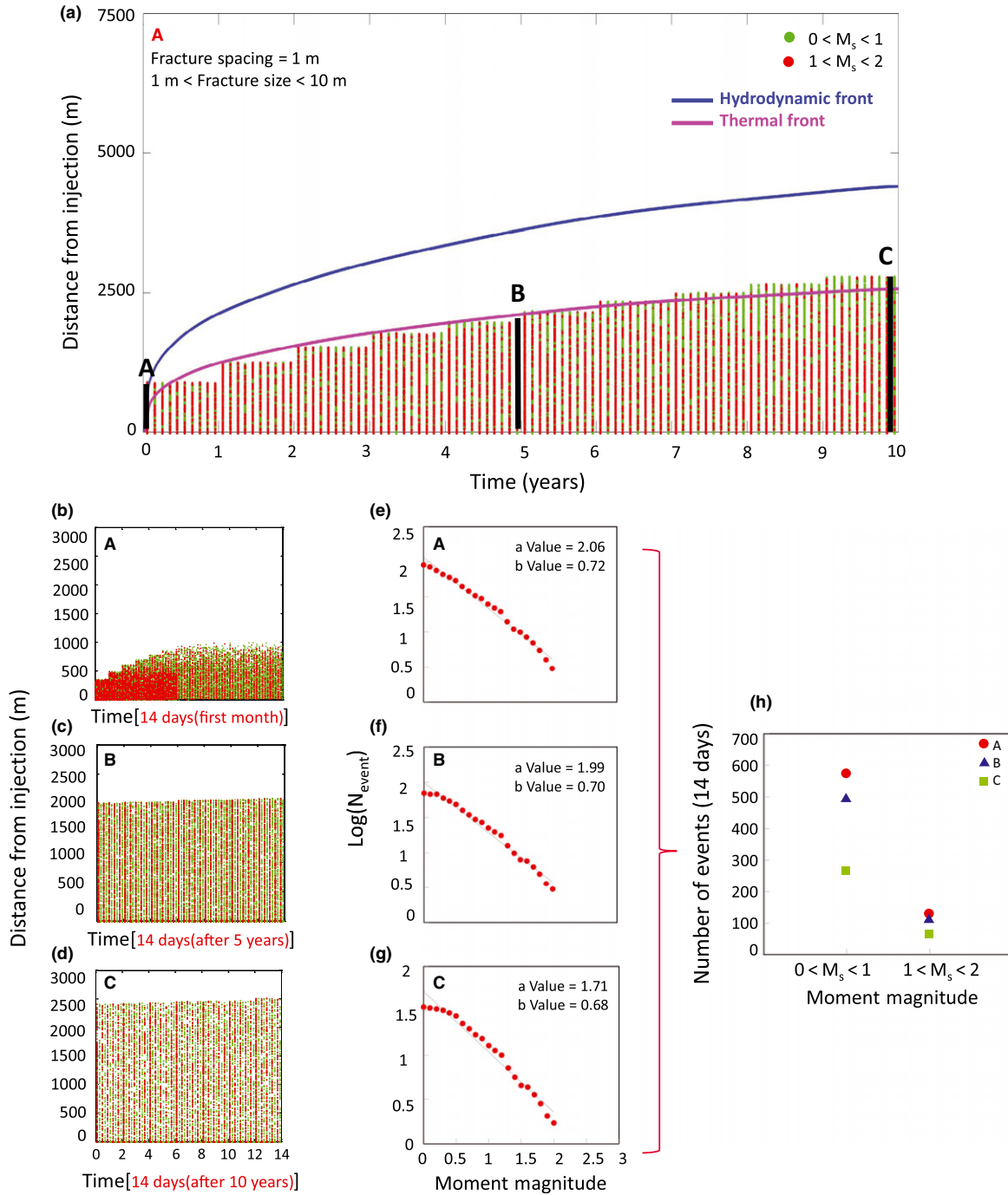


**Fig. 6** (a) Radius vs. time plot for short term of the progress of fluid and thermal fronts in the reservoir and of induced seismicity after 10 years production (injection flow rate is 15 l/s). Seismic moment of individual events shown green (smaller event):  $0 < M_s < 1$  and red (larger event):  $1 < M_s < 2$ . The hydrodynamic front illustrated with blue and thermal front with pink solid line. Fracture density is  $\sim 0.1 \text{ m}^{-1}$  (fractures are in the ranges of 1–500 m, fracture spacings are in the ranges of 10–500 m). We separately zoom in on three windows (considering 2 weeks period at each window) A, B and C at three different times (14 days after stimulation, after 5 years and after 10 years). (b) Seismic activity at early time (2 weeks period). (c) Seismic activity after 5 years production (2 weeks period). (d) Seismic activity after 10 years production (2 weeks period). (e, f, g) number of events as a function of magnitude indicating  $b$ -value of 0.72 at early time, 0.7 after 5 years and 0.68 after 10 years production (moment magnitude range 0–2). (h) Number of events as a function of moment magnitude for three different times (first month, 5 and 10 years). The number of events with small ( $0 < M_s < 1$ ) and large ( $1 < M_s < 2$ ) magnitude shows in three different colours; red, blue and green. Red, number of events at the stimulation period; blue, number of events after 5 years production; green, number of events after 10 years production.

The  $b$ -value is an important parameter for the estimation of earthquake hazard. The  $b$ -value is related to the rock type and the state of stress and increases with the ductility of the rock (Scholz, 1986).

The modelled  $b$ -value represents the cumulative number of seismic events at each location within the reservoir with the local magnitude evaluated from its seismic moment. Gutenberg & Richter (1944) expressed the magnitude distribution in the form  $\log N_{\text{event}} = a - bM$ , where  $N_{\text{event}}$  is the number of seismic events within a magnitude interval  $M \pm \Delta M$ . Here, we discuss the scaling of the frequency of events  $N_{\text{event}}$  as a function of fluid pressure and temperature. The magnitude–frequency relation evaluated at early time (first month) is illustrated in Fig. 5 – left. The approximate  $b$ -value is  $\sim 0.7$  and this is constrained only by an assumed fracture density. The shape of the resulting frequency–magnitude distribution is similar to that reported for the Cooper Basin (Baisch *et al.*, 2009; Shapiro and Dinske, 2009b) and the evaluated  $b$ -value in particular matches the Habanero-1 well data. The histogram of event magnitudes, which was determined for the 2005 data catalogue, indicates a  $b$ -value of 0.8 in the magnitude range  $-0.8$  to  $+1.5$  (Baisch *et al.*, 2009) and the approximate  $b$ -value from Shapiro and Dinske (2009b) is  $+0.75$ . Events migrate during the simulated evolution due to the progress of fluid pressure diffusion. For this particular reservoir, the microseismicity begins at the injector and migrates upwards with time. From the Gutenberg–Richter relation, from Aki's (1981) supposition and from our observations, we conclude that the  $b$ -value describes fracturing processes in the seismic region and is related to the size, location, distribution and spacing of fractures.

#### Effect of hydrodynamic and thermal front on triggered seismicity

The numerical model is used to follow the hydrodynamic and thermal fronts as they propagate through the reservoir. The data used in this simulation are related to the Cooper Basin EGS, which is also discussed elsewhere (Shapiro and Dinske, 2009a).

The location of these fronts is defined by the propagation of the fluid flow rate at any given time within the TOUGHREACT module (Xu *et al.*, 2006). The evolution of seismicity for 10 years reservoir production is shown in a radius–time plot relative to the propagation of these fluid and thermal fronts in Fig. 6a (injection flow rate is set at 15 l/s in the simulation). This shows the progress of the fluid and thermal fronts in the reservoir together with the progress of induced seismicity. We observe that the rate of propagation of the hydrodynamic front is approximately twice as rapid as the thermal front.

This illustrates that most of the seismic activity is triggered by hydraulic effects at early times (days to month) relative to the initiation of stimulation. At later time (month to years), thermal effects specifically, or chemical effects possibly, may contribute to the seismicity when the seismicity front lags behind the hydrodynamic front due to small changes in pressure. By following the propagation of both fluid pressure and thermal fronts through the reservoir with time, we associate large early-time events with the fluid front and the lower seismic magnitude later-time events with the transit of the thermal/chemical front.

Then, we confirm the form of observations in our model against those reported in Shapiro and Dinske (2009a), which in turn has been calibrated against field data. We observe good agreement between our model observations and those in the Cooper Basin (Shapiro and Dinske, 2009a,b). We then compare the magnitude–frequency relations evaluated for the Cooper Basin stimulation at three different times, Fig. 4 (first month followed by after 5 and 10 years). We considered a 14-day window at each time frame to normalize the number and magnitude of events at any location within the reservoir Fig. 4. The number of events as a function of time is controlled only by the cumulative mass of fluid injected, which then results in failure and energy release. The larger this energy release, the larger number of seismic events induced at a given location and time.

Also, we characterize the induced seismicity by the  $b$ -value for these different time periods. The approxi-

mate  $b$ -value is illustrated in Fig. 4 and corresponds closely with observations. The plot of event magnitudes determined here indicates a  $b$ -value of 0.72 in the magnitude range 0 to  $+2$  at early time,  $+0.7$  after 5 years and  $+0.68$  after 10 years. This behaviour shows that the  $b$ -value is highest at early time and means that the larger events occur earliest (days to month) and due to the passage of the fluid pressure front. At later times (month to years), the principal factor triggering the seismicity is thermal effects. Finally, in Fig. 4, we illustrate the number of event at each time. It shows that the largest number of seismic events exists for  $0 < M < 2$  induced near injection and decreases away from the point of injection.

#### Conclusion

We explore the coupling between THMC behaviours on fractured reservoirs to understand the critical processes during the thermal recovery from EGS reservoirs. Large fractures (faults) with infill fractures (small–large) of various spacing, orientation and fracture placement represent the distributed fracture network within the reservoir. We use this distribution for a fractured geothermal reservoir in the Cooper Basin to understand the significant behaviours of THMC effects on fractured reservoirs. The activated fractures due to pore pressure propagation and induced thermal and chemical strains can generate different failure regimes in the reservoir and the incremental development of energy release of fractures can induce seismic events with varying ranges of magnitude ( $-3$  to  $5$ ) at short and long time-scales.

We capture the energy release of fractures and then the magnitude is utilized to obtain the magnitude–moment relation and to compare our model with the measured  $b$ -value that observed at early-time reservoir stimulation (2 weeks) to understand the induced seismicity at the Cooper Basin. This is then extended to explore the evolution of seismicity expected over an extended period of production (10 years).

Events occur from energy release on seeded fractures enabling moment magnitude, frequency and spatial

distribution to be determined with time. We evaluated the magnitude of events and it varies from  $-2$  to  $+2$  and the largest event size ( $\sim 2$ ) corresponds to the largest fracture size ( $\sim 500$  m), which represents the weakest planes within reservoir and a prescribed stress drop of 9 MPa.

We separately examine the impact of thermal stresses, pore pressure and chemical effects on the evolution of seismicity during this long-term production. The most important mechanism, which triggers slip and promotes seismic events along the weak planes and also may change the moment, is the augmentation of fluid pressure at early time. However, with migration of fluid in the fractures at later time, thermal quenching can cause a reduction in effective stress and additionally contribute to triggered seismicity.

Modelled  $b$ -values ( $\sim 0.6$ – $0.7$ ) also correspond to observations ( $\sim 0.7$ – $0.8$ ) and this approach is verified using data for the Cooper Basin (Australia) geothermal field. We tracked the hydrodynamic and thermal fronts to define causality in the triggering of seismicity.

To describe the reservoir from valid data, we tried to find a good correlation among spacing, length, orientation and placement of fractures in the model and then calibrate the model by replicating observed  $b$ -values during reservoir production. The  $b$ -value describes the fracture process within reservoirs and is related to size, location, distribution and spacing of fractures.

Finally, we illustrate the penetration of hydrodynamic and thermal fronts through the reservoir with time. The hydrodynamic front moves twice as fast as the thermal front and envelopes the triggered seismicity at early time (days to month) – with higher flow rates correlating with larger magnitude events. For later time ( $>1$  year), thermal drawdown and potentially chemical influences principally trigger the seismicity, but result in a reduction in both the number of events and their magnitude.

### Acknowledgements

This study is the partial result of support from the Department of Energy Office of Energy Efficiency and Renewable Energy and Geothermal Technology Program under contract EE-10EE0002761. This support is gratefully acknowledged.

### References

- Aki, K., 1967. Scaling law of seismic spectrums. *J. Geophys. Res.*, **72**, 1217–1231.
- Aki, K. 1981. A probabilistic synthesis of precursory phenomena. In: *Earthquake Prediction*, (D.W. Simpson and P.G. Richards, eds), pp. 566–574. Am. Geophys. Union, Washington D.C.
- Baisch, S., Weidler, R., Vörös, R., Wyborn, D. and Graaf, L., 2006. Induced seismicity during the stimulation of a geothermal HFR reservoir in the Cooper Basin, Australia. *Bull. Seismol. Soc. Am.*, **96**, 2242–2256.
- Baisch, S., Vörös, R., Weidler, R. and Wyborn, D., 2009. Investigation of fault mechanisms during geothermal reservoir stimulation experiments in the Cooper Basin, Australia. *Bull. Seismol. Soc. Am.*, **99**, 148–158.
- Barton, N., Bandis, F. and Bakhtar, K., 1985. Strength, deformation, and conductivity coupling of rock joints. *Int. J. Rock Mech. Min. Sci.*, **22**, 121–140.
- Brune, J. and Thatcher, W., 2002. *International Handbook of Earthquake and Engineering Seismology*, vol. **81A**. International Association of Seismology and Physics of Earth's Interior, Committee on Education, pp. 569–588.
- Elsworth, D. and Yasuhara, H., 2010. Mechanical and transport constitutive models for fractures subject to dissolution and precipitation. *Int. J. Num. Meth. Geomechs.*, **34**, 533–549.
- Goodman, R.E., 1976. *Methods of Geological Engineering in Discontinuous Rocks*. West Publishing, New York, 472 pp.
- Grasso, J.R. and Wittlinger, G., 1990. 10 years of seismic monitoring over a gas field area. *Bull. Seismol. Soc. Am.*, **80**, 450–473.
- Gutenberg, R. and Richter, C.F., 1944. Frequency of earthquakes in California. *Bull. Seismol. Soc. Am.*, **34**, 185–188.
- Hubbert, M.K. and Rubey, W.W., 1959. Role of fluid pressure in mechanics of overthrust faulting 1. Mechanics of fluid-filled porous solids and its application to overthrust faulting. *Geol. Soc. Am. Bull.*, **70**, 115–166.
- Kanamori, H., 1977. The energy release in great earthquakes. *J. Geophys. Res.*, **82**, 2981–2987.
- Keylis-Borok, V.I., 1959. On estimation of the displacement in an earthquake source and of source dimensions. *Ann. Geofisic.*, **12**, 205–214.
- Kovac, K.M., Xu, T., Pruess, K. and Adams, M.C., 2006. Reactive chemical flow modeling applied to injection in the Coso EGS experiment. In: *Proceedings of the 31st workshop on geothermal Reservoir engineering*, Stanford University.
- Majer, E.L. and Peterson, J.E., 2007. The impact of injection on seismicity at The Geysers, California Geothermal Field. *Int. J. Rock Mech. Min.*, **44**, 1079–1090.
- Majer, E.L., Baria, R., Stark, M., Oates, S., Bommer, J., Smith, B. and Asanuma, H., 2007. Induced seismicity associated with enhanced geothermal systems. *Geothermics*, **36**, 185–222.
- Purcaru, G. and Berckemer, H., 1978. A magnitude scale for very large earthquakes. *Tectonophysics*, **49**, 189–198.
- Scholz, C.H., 1986. The frequency-magnitude relation of microfracturing in rock and its relation to earthquakes. *Bull. Seism. Soc. Am.*, **58**, 399–415.
- Segall, P., 1989. Earthquakes triggered by fluid extraction. *Geology*, **17**, 942–946.
- Shapiro, S.A. and Dinske, C., 2009a. Fluid-induced seismicity: pressure diffusion and hydraulic fracturing. *Geophys. Prospect.*, **57**, 301–310.
- Shapiro, S.A. and Dinske, C., 2009b. Scaling of seismicity induced by nonlinear fluid-rock interaction. *J. Geophys. Res.*, **114**, B09307.
- Taron, J. and Elsworth, D., 2009. Thermal-hydrologic-mechanical-chemical processes in the evolution of engineered geothermal reservoirs. *Int. J. Rock Mech. Min. Sci.*, **46**, 855–864.
- Taron, J., Elsworth, D. and Min, K.B., 2009. Numerical simulation of thermal-hydrologic-mechanical-chemical processes in deformable, fractured porous media. *Int. J. Rock Mech. Min. Sci.*, **46**, 842–854.
- Walsh, J.B., 1965. Effect of cracks on uniaxial elastic compression of rocks. *J. Geophys. Res.*, **70**, 399–411.
- Xu, T. and Pruess, K., 2001. Modeling multiphase non-isothermal fluid flow and reactive geochemical transport in variably saturated fractured rocks: 1. *Methodology. Am. J. Sci.*, **301**, 16–33.
- Xu, T. and Pruess, K., 2004. Numerical simulation of injectivity effects of mineral scaling and clay swelling in a fractured geothermal reservoir. Report LBNL-55113, Lawrence Berkeley National Lab, Berkeley.
- Xu, T., Sonnenthal, E., Spycher, N. and Pruess, K., 2006. TOUGHREACT—a simulation program for non-isothermal multiphase reactive geochemical transport in variably saturated geologic media: applications to geothermal injectivity and CO<sub>2</sub> geological sequestration. *Comput. Geosci.*, **32**, 145–465.
- Yerkes, R.F. and Castle, R.O., 1976. Seismicity and faulting attributable to fluid extraction. *Eng. Geol.*, **10**, 151–167.

Received 14 March 2012; revised version accepted 13 March 2013